Journal of Saudi Chemical Society (2019) **23**, 427–438

King Saud University

Journal of Saudi Chemical Society

www.ksu.edu.sa
www.sciencedirect.com

ORIGINAL ARTICLE

BPB dye confined growth of surfactant-assisted mesostructured silica matrix fiber optic sensing tracers

Shumaila Islam [a], Hazri Bakhtiar [a,*], Zuhaib Haider [a], Saira Riaz [b], Shahzad Naseem [b], Kashif Chaudhary [a], Lau Pik Suan [a], Siti Sarah Usman [a], Muhammad Safwan bin Abd Aziz [a]

[a] *Laser Centre, Ibnu Sina Institute for Scientific and Industrial Research, Universiti Teknologi Malaysia, Skudai, Johor 81310, Malaysia*
[b] *Centre of Excellence in Solid State Physics, University of the Punjab, Lahore, Pakistan*

Received 7 February 2018; revised 27 July 2018; accepted 30 July 2018
Available online 10 August 2018

KEYWORDS

Silica nano-matrix;
Bromophenol blue dye;
Mesoporous structure;
Optical properties;
Evanescent field optical fiber sensors;
Sensitivity

Abstract Thermally stable surfactant modified silica nano-matrix is synthesized by the sol–gel method at low temperature. The surfactant such as cetyltrimethylammonium bromide (CTAB) assisted silica matrix is encapsulated with bromophenol blue (BPB) for sensing activities. Prepared nano-matrix consists of numerous morphological structures such as a pseudo-spherical, hierarchal and islands. The morphology of mesoporous high surface area matrices is strongly affected by CTAB, BPB dye and the aging conditions that determine the transformation from disordered silica nano-matrix morphologies to ordered encapsulated structures. Furthermore, smooth surface matrices with low surface roughness 1.2 nm, low refractive index 1.36, large pores and small dimensions of heteroatoms contribute to the stable sensing activities. The response of coated fiber optic is determined at dynamic pH range 1–12. The prepared sensor has reversibility/repeatability, stability and fast response time of approximately 0.25 s in basic media. The accuracy of sensing device measurements in household ammonia solution and the borax solution suggested that prepared device has clear potential for daily life usage.

1. Introduction

Recently, silica-based materials have received a great attention for the synthesis of nano- and/or mesostructured materials with ultra-porous networks and the high surface area in a wide range of research fields such as energy conversion and storage, adsorption, catalysis, and sensor technology [1–3]. In particular, silica-based nanomaterials have combined advantages of

* Corresponding author.
E-mail addresses: hazri@utm.my (H. Bakhtiar), safwanaziz@utm.my (M.S.bin.A. Aziz).
Peer review under responsibility of King Saud University.

Production and hosting by Elsevier

https://doi.org/10.1016/j.jscs.2018.07.005
1319-6103

organic functionalities with inorganic oxides. A characteristics due to superior properties of silica i.e., high colloidal stability, chemically inertness, thermal stability, water-solubility, non-toxicity, biocompatibility, transparent to light, magnetism (allowing the combined components to keep their original optical and/or magnetic properties) that makes it an ideal support for encapsulation of organic and inorganic nanomaterials [4–6]. In some cases, the interaction between the metal and organic species consists of non-bonded interactions due to electrostatic bonding, hydrogen bonding, and van der Waals forces. This type of non-covalent organically modified silicates contains chemical moieties to increase compatibility [7]. However, sol–gel based composites' formation relies on the covalent bonds chemistry between the two systems to increase phase coupling [8]. So far, the wet chemical route i.e., sol–gel is the most frequently employed method for silica-based composite preparation at mild conditions due to its convenient control over shape, size, and structures [9].

The structures of the composites have a decisive significance for their properties and applications. Regular morphology with controllable size of silica nanoparticles cannot be obtained easily. During aging period, large particles crack due to volatile components' evaporation and smaller particles are unstable that tend to aggregate. As demonstrated in many studies, smooth crack-free morphological control is a critical factor, especially for sensing applications. Uniform/ordered and spherical morphology attracts sustained research interests because it minimizes the viscous effects and provides short pathways for transport and controlled diffusion of reagents and analytes [1]. In pH sensors, stability and leachability from porous supports (matrix), which host the dye, is also a critical issue. Therefore, large-sized mesopores, smooth mass transport can be grasped for large reagent molecules. Coti et al. [10] reported that due to the organic appendages on the surfaces of the nanoparticles and onto the walls of the pores, mesoporous silica is considered as a highly suitable host material for the incorporation of guest molecules (dye). For this study, BPB dye molecules are encapsulated in silica matrix. TEOS is used as silica source which is hydrophilic and the resultant matrix is negatively charged. Basically, the nature of the matrix affects virtually all characteristics and applications of the dye, such as it causes spectral shifts of both absorption and emission; it affects the intersystem crossing, and consequently sensing lifetime [11].

Lately, many cladding-removed optical fiber (CROF) based approaches have been developed for detecting humidity [12–14], ethanol [15], methanol [16], ammonia [17], and other gases [18,19]. Nevertheless, as it was previously commented, optical fiber sensors are gaining the interest of the scientific community by their already well-known advantages such as remote sensing, small dimensions, low weight, immune to electromagnetic interferences, real-time monitoring, biocompatibility, and multiplexing capabilities [20]. The use of nanoparticles in coatings, its fabrication, parameters, and compositions are still under study in order to improve sensitivity, stability, and other desirable sensing values. Generally, for optical fiber sensing, cladding-removed optical fiber (CROF) is one of the simplest structures, operated on the modulation of the light intensity propagating in the fiber. The advantage of intensity based plastic clad silica (PCS) pH sensor lies in their simplicity and compatibility with multi-mode fiber technology providing greater sensitivity than direct spectroscopic devices [21]. A short distance of the fiber cladding is removed and then replaced by the nanostructured coating (sensitive region), which interacts with the surrounding media. Additionally, the combination of fiber optic with the dye encapsulated matrix can enhance certain performance parameters of the existing devices, e.g., dynamic range, sensitivity, robustness, and lifetime. These improvements are due to the mesoporosity, high surface area and lower roughness of host matrix. Thus, a higher surface area in sensitive regions allows even lower limits of detection in pH sensing. Furthermore, the encapsulation of dyes into mesoporous network is a considerable challenge due to its leaching problems, dynamic range and response time; numerous efforts have been directed toward the development of non-leaching and fast responsive pH sensors at dynamic pH range, which is summarized in Table 1.

Table 1 pH range and response time of BPB encapsulated silica matrix.

pH sensitivity range	Response time	Ref.
2–4	–	[22]
4–7.5	–	[23]
3–6	Several minutes	[24]
2–12	15–150 s	[25]
3–5	1–2 min	[26]
3–8	20–40 s	[27]
5–7	10 s	[28]
4–7.5	5 s	[29]

Hereby, we are reporting the possibility of introducing BPB dye into the smooth crack-free mesoporous silica network that modified the morphology, physiochemical and optical properties of the nano-matrices for broad dynamic pH range and fast responsive fiber optic pH sensing applications. Experimental analysis suggested that silica-based nanocomposites with smaller size and various structures can be obtained by surfactant CTAB addition (structure modifying agent) and by the appropriate aging period, it is possible to achieve complete entrapment thereby eliminating leaching and fast response of prepared sensor can be observed.

2. Experimental

2.1. Chemicals and reagents

Tetraethylorthosilicate (TEOS) [98% Aldrich], ethanol (EtOH) [Grade GC, 94%, QRec], nitric acid (HNO3) [65% Merck], cetyltrimethylammonium bromide (CTAB) [Fisher Chemicals], bromophenol blue (BPB) [Merck], and standard pH buffer solutions were purchased from Sigma–Aldrich. All these products were used exactly as received without further purifications.

2.2. Synthesis of the silica nano-matrix and BPB encapsulated silica matrix sols

Silica sol was synthesized by mixing optimized values of 10 ml TEOS (tetraethylorthosilicate) into 40 ml ethanol and mixture of 20 ml H_2O and 2 ml of 0.1 M HNO_3. The molar ratios were TEOS: EtOH: H_2O: $HNO_3 \sim 1.38: 5.5: 2.7: 0.27$. According to literature [30], in open system, ethanol is more volatile than

water, which decreases the re-esterification reaction probability and leads to enhance the hydrolysis rate. Whereas, the high ratio of water reduces the aggregation between the silanol groups Si (OH) and favors long gelation time. Moreover, 1 ml of 0.5 M concentration of Cetyl Trimethyl Ammonium Bromide (CTAB) solution was mixed into the above solution. The solution was stirred for 1 h at 70 °C. On the other hand, BPB encapsulated silica matrix was synthesized by mixing of 2 ml of 0.05 M concentration of BPB dye into silica sol. This mixture was stirred and heated at 80 °C for 1 h. In order to ensure proper combination of the constituents and removal of volatile components from synthesized sol, it left for several days for appropriate aging cycles at room temperature. The overall scheme reaction for nanoporous network with schematic illustration is shown in Fig. 1.

2.3. Sensor device preparation

For fiber optic sensing device, processing steps were as follows: firstly, ~5 cm unclad portion of the PCS optical fiber (25 cm long, 1012 µm core diameter with NA = 0.37 ± 0.02 and 1.457 core refractive index) was cleaned for 5 min by concentrated nitric acid. Secondly, after thoroughly rinsing with deionized water, the sol was dripped off (drop casting) on unclad portion of the fiber (a drop of the solution is hold at the exit of a needle, and then, the drop is moved along the 5 cm unclad segment of fiber). The same conditions were adopted for glass substrates. After drop casting, the substrates i.e., glass slides and fiber were aged at room temperature for several days. The BPB encapsulated silica nano-matrix were self-assembled on the surface of the sensing fiber because of the electrostatic force produced. Subsequently, the modified optical fiber was treated with buffer solution pH 1–12.

3. Characterization

Field-emission scanning electron microscopy (FESEM, Carl Zeiss) was employed to observe the morphology of the prepared samples. Whereas, energy dispersive X-ray (EDX) was used to analyze the elemental constituents of silica nano-matrix and BPB encapsulated silica matrix. The roughness was analyzed by atomic force microscopic (AFM) equipment SPI 3800N. FTIR spectrophotometer Perkin Elmer Series L160000A (in the range of 4000–450 cm^{-1}) was used to assess the structural information and interaction between the reactive species and silica molecules. Silica nano-matrix and BPB encapsulated silica matrix specific surface area was measured by Brunauer–Emmett–Teller (BET) method using micromeritics 3 Flex version 3.01. Average pore size distribution of prepared samples was calculated by Barrett–Joyner–Halanda (BJH) model. UV–visible transmission spectra of silica nano-matrix and BPB encapsulated silica matrix thin films were measured by Shimadzu UV-3101PC spectrophotometer. The employed spectra were in the range of 400–700 nm with an accuracy of ± 3 nm. Weight loss and behavior of the prepared silica nano-matrix and BPB encapsulated silica matrix at high temperatures were investigated by Thermo gravimetric analysis. The analysis was carried out with a heating rate of 10 °C/min from room temperature to 300 °C with Mettler Toledo Srar thermal analysis system (Versions 9.10 and 9.20). The progressive response of sensor for dynamic pH range 1–12 was inspected by an experimental setup system. The setup sys-

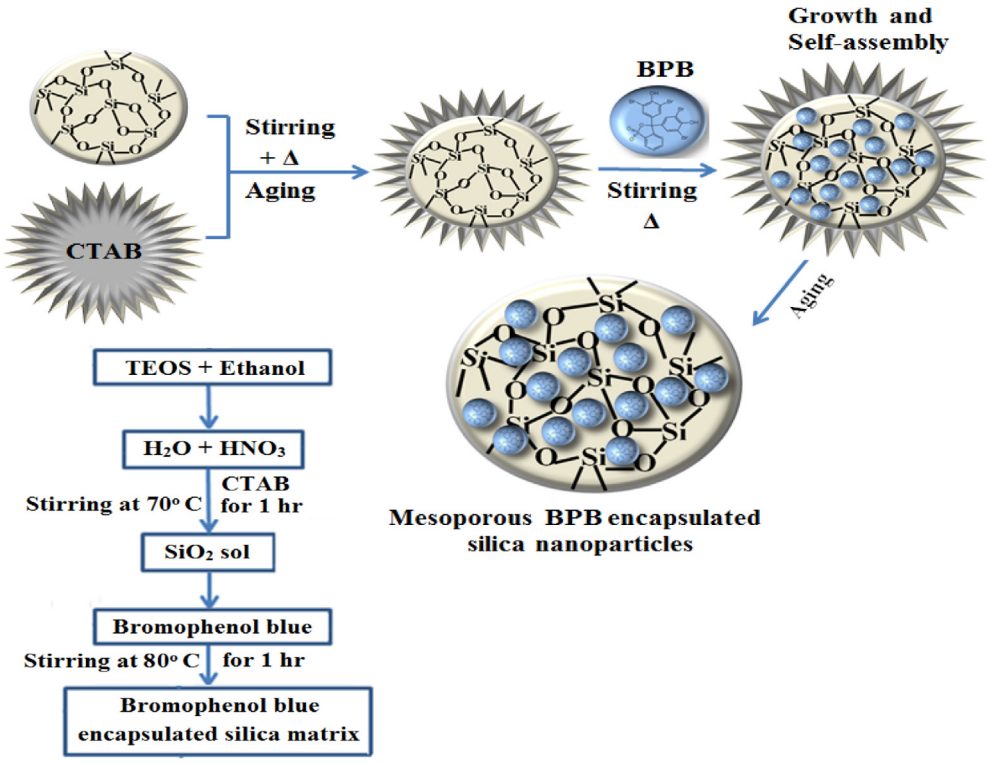

Fig. 1 Overall scheme reaction of silica nano-matrix and BPB encapsulated silica matrix, schematic representation of proposed mechanism for synthesized BPB encapsulated silica porous matrix network.

tem consists of the white LED as light source, a scientific-grade UV–Vis spectrometer (USB2000, Ocean Optics Inc., Dunedin, FL, USA) and a data processing computer. The transmitted light was then collected by spectrometer in terms of light intensity toward the wavelength with associated data processing software (Spectra Suite, Ocean Optics Inc., Dunedin, FL, USA).

4. Results and discussions

4.1. Structural analysis

FE-SEM analysis was employed in order to assess the influence of CTAB on silica matrix and behavior of encapsulated BPB dye species into silica matrix morphology. Fig. 2-I(a) shows overall heterogeneous morphologies of silica particles at lower magnification 20 μm. However, magnified micrographs [Fig. 2-I(b–d)] show the coalescence of nano-colloids of CTAB modified silica particles clearly, which is probably due to the uncontrolled agglomeration of nanoparticles. Generally, silica particles have tendency to easily agglomerate because of their large surface-to-volume ratios and high surface tension. Formation of silica was increased by following the continuous reduction of silica ions. In order to diminish its considerably high surface energy, it starts to coalesce in an oriented fashion instead of further growing individually [Fig. 2-I(c)]. Inset (i) is a schematic representation of CTAB modified silica particles. Ataee-Esfahani et al. [2] reported that interaction between the silica particles and surfactant species through hydrogen bonding allows the molecules to organize into an ordered array at the liquid–solid interface, thus generating mesoporous structures. Fig. 2-I(d) is corresponding to the magnified area of (c) which clearly shows porous nature of silica matrix. During aging, exchange reactions take place

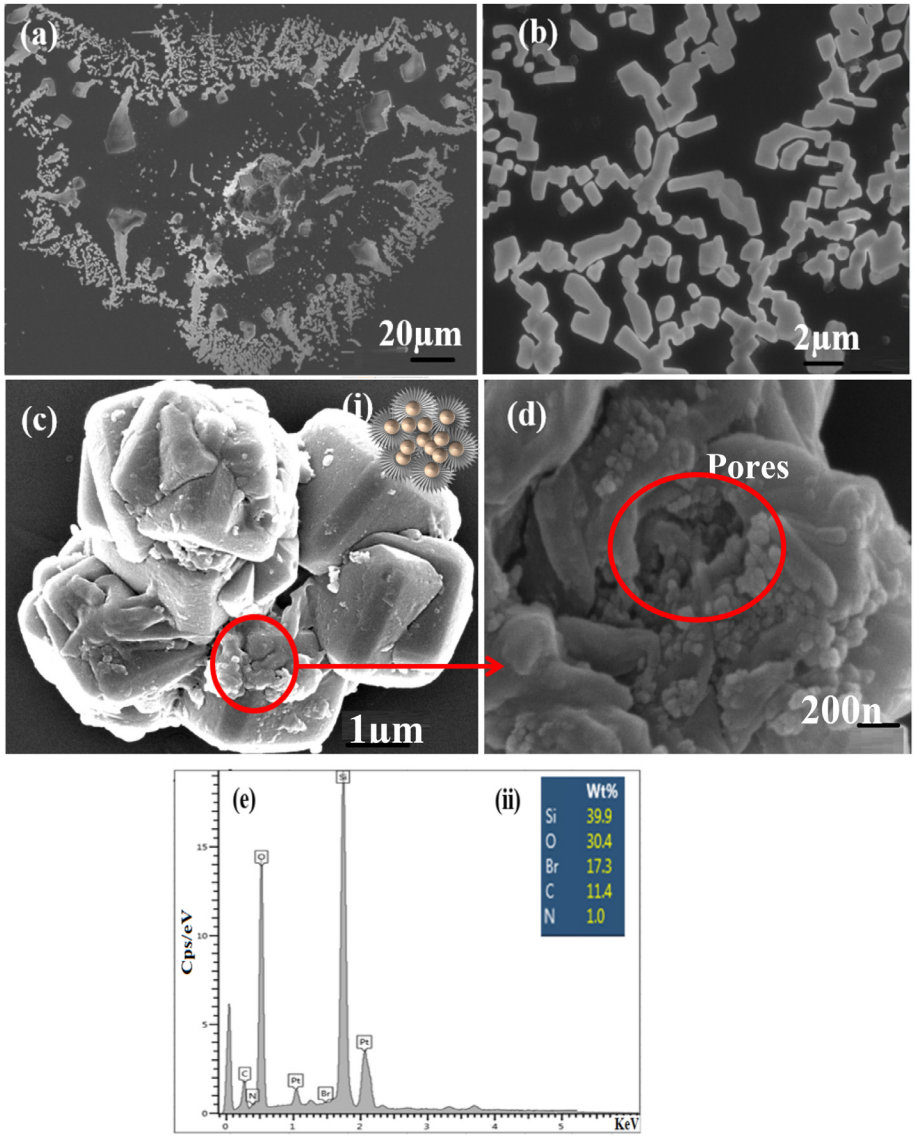

Fig. 2-I (a) FE-SEM micrographs of CTAB assisted silica nano-matrix, (b, c) is the magnified area of (a), whereas, (d) is corresponding to the magnified area of (c). While, inset (i) corresponding to the schematic representation of CTAB assisted silica nano-matrix, (e) is EDX spectrum of (a), and (ii) is wt. % values of CTAB assisted silica nano-matrix elements.

(hydrolysis of ethoxy groups and polycondensation of the resulting species), thus leading to the formation of small crystallites with a high surface-to-volume ratio [Fig. 2-I(d)].

Furthermore, dispersal state of the CTAB-modified silica matrix after encapsulation was observed in Fig. 2-II(a); may be dye species stabilized sufficiently to ensure a degree of order in the CTAB assisted silica porous network. Fig. 2-II(b) is the magnified image of Fig. 2-II(a); the nanoparticles are nucleated/grown [31], suggesting that the surfactant CTAB can be used to obtain non-aggregated, nano-porous channel structures of BPB encapsulated silica matrix. Inset (i) is representing a schematic illustration of BPB encapsulated CTAB modified silica matrix. Generally, the physical status/properties and behavior of encapsulated BPB dye molecules in a silica nano-matrix is affected by three major factors—aggregation, restricted motion and limited diffusion. After encapsulation, less aggregation was observed between dye molecules and silica nano-structure (contains —Si—O—Si— bonds) [Fig. 2-II(c)]. As documented in literature [32], the molecules motion can be hindered in rigid polymer matrices or in viscous media. In silica nano-matrix, —O—Si—O— chains act like a barrier to reduce their motion between the dye molecules, thus reducing the possibility of aggregation. High concentration of dye molecules in the silica matrix results in the formation of high degree of aggregates. In addition, particles are uniformly arranged after encapsulation and result in a flower-shaped compact framework. However, some alveolate pores were also observed [Fig. 2-II(d)]. These pores are caused by the removal of the organic compounds (solvent and CTAB species) from the silica particles. Distribution of pores/porosity channels was developed as a result of differential stresses developed from non-uniform drying/shrinkage/evaporation of organic solvents or from CTAB. Such differential stresses arising from inhomogeneous densification and are associated with brittle transition in

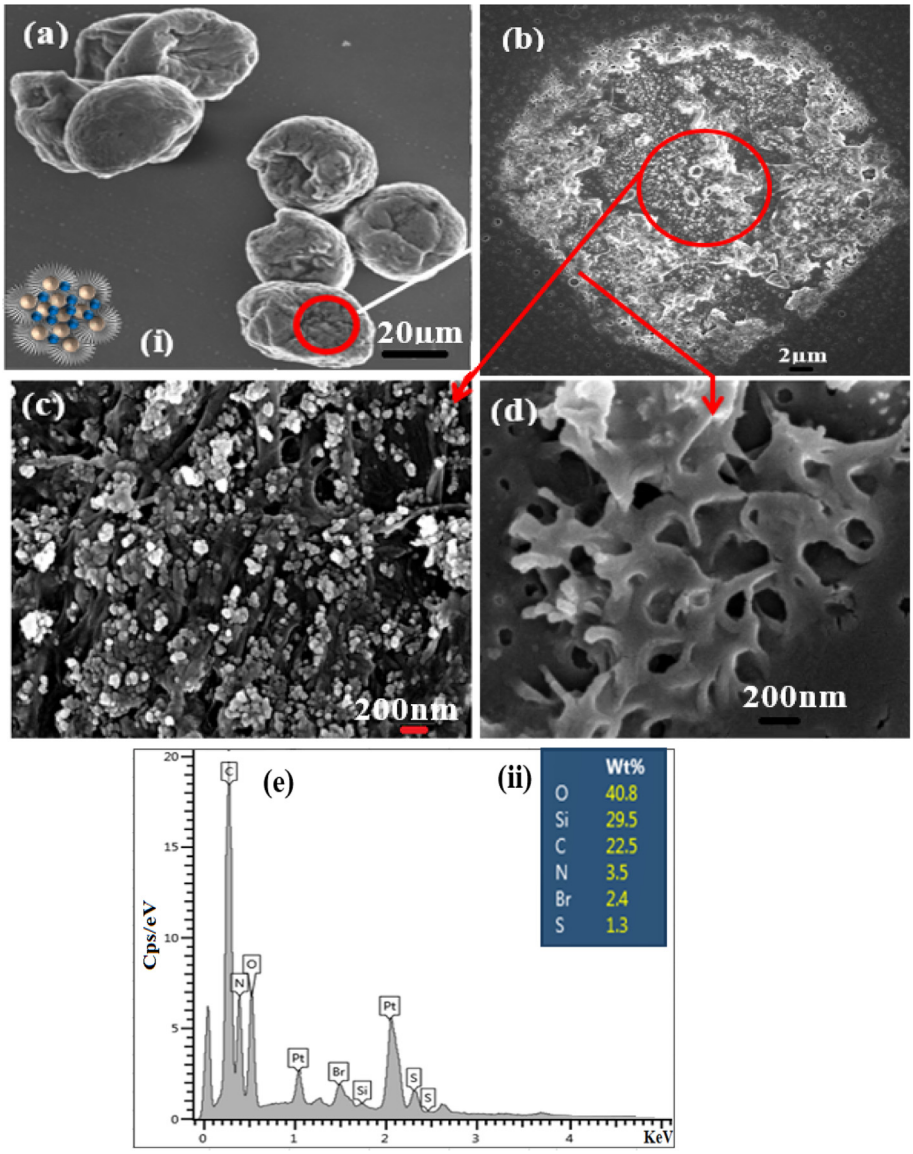

Fig. 2-II (a) FE-SEM micrographs of BPB encapsulated CTAB modified silica particles, (b) is the magnified area of (a), whereas (c, d) is zoomed area of (a). (e) corresponding to the EDX spectrum of (a), inset (i) is a schematic representation of BPB encapsulated CTAB modified silica matrix and (ii) is wt. % values of elements.

consolidated bodies, and can yield the crack propagation if not relieved properly. Moreover, some other structural defects and pores associated with density variations can play a detrimental role by growing during heat treatment and thus limiting end-point densities.

Fig. 2 [I(e) and II(e)] shows the EDX spectra of silica nano-matrix and BPB encapsulated silica matrix, respectively. Pt signals belong to the top coating, which was applied for FE-SEM analysis. Both samples exhibited silicon, oxygen, carbon, nitrogen and bromine signals, the values in wt. % are tabulated in insets of Fig. 2-I and II(e). Presence of these elements suggests that the nanoparticles are only made up of Si and O. Carbon, nitrogen and bromine is associated with CTAB. Moreover, oxygen and carbon also correspond to BPB species. After encapsulation, slight variations of elements were observed which reveals that the CTAB and BPB species has good interaction with silica network.

Atomic force microscopy (AFM) analysis was carried out to study the morphological characteristics/texture, average surface roughness (Ra) and root mean square surface (RMS) roughness of silica nano-matrix and BPB encapsulated silica matrix. The scanned area is 1x1 μm^2. Fig. 3(a, b) illustrates the 3-D topography of silica nano-matrix and BPB encapsulated silica matrix, respectively, signifying the locally homogeneous surfaces, spherical shape and nano-scale size distribution of resultant nanoparticles.

The 2-D view and its respective line profile of silica nano-matrix [Fig. 3(c)] and BPB encapsulated silica matrix [Fig. 3 (d)] shows the representative overall length of marked particles. 3-D image of CTAB assisted silica nano-matrix [Fig. 3 (a)] suggests the porous aggregated structure morphology and measured Ra is ~1.73 nm with RMS roughness ~2.2 nm. However, after encapsulation Ra is decreased down to 1.2 nm and RMS down to ~1.44, and monodispersity of particles highlights the good interaction of dye species with silica nano-matrix [Fig. 3(b)]. Once BPB dye is encapsulated into the mesoporous silica network, the flat and rigid dye species can no longer escape and remain well trapped within the silica network. Subsequently, the interaction of BPB dye species and CTAB micelle may generate π-stacking, and such phenomenon could emphasize the stability of dye toward encapsulation and enhance the rigidity of the structure. Moreover, the π-stacking ordering of the dye species favors their insertion into the silica network and therefore enhances the encapsulation process [33].

FT-IR spectra of silica nano-matrix and BPB encapsulated silica matrix are shown in Fig. 4(a, b), whereas, inset (I) corresponding to the BPB dye spectrum. The characteristic vibrations of Si—O were observed at 467 cm^{-1}, 798 cm^{-1} and 966 cm^{-1} in both samples, silica has transverse-optic (TO) stretching bonds of SiO_4 tetrahedron [34]. The band at ~1093 cm^{-1} is associated with the transverse optical vibration mode corresponding to the asymmetric stretching of the inter-tetrahedral oxygen atoms in the Si—O—Si linkage. However, after encapsulation, siloxane-stretching vibration became wider and shifted to 1099 cm^{-1}, this peak broadening and shifting may be associated with the strong electrostatic interaction between the positive surface group of silica and the negative functional groups (—OH^-, —COO^-, —SO_3^-) of BPB dye, as documented in the literature [35]. On the other hand, the sharp signal at 1381 cm^{-1} is associated with the asymmetric/symmetric stretching of nitrogen-oxy/C—N from CTAB. Bending vibrations and stretching vibrational modes around ~1641 cm^{-1} and ~3398 cm^{-1} are associated with surface –OH groups. According to the literature [35], the broadening and shifting of ~3398 cm^{-1} band after encapsulation than BPB dye and silica matrix indicates the formation of hydrogen bonding between surface OH groups of silica and the functional –OH groups of BPB dye molecules. Furthermore, peaks

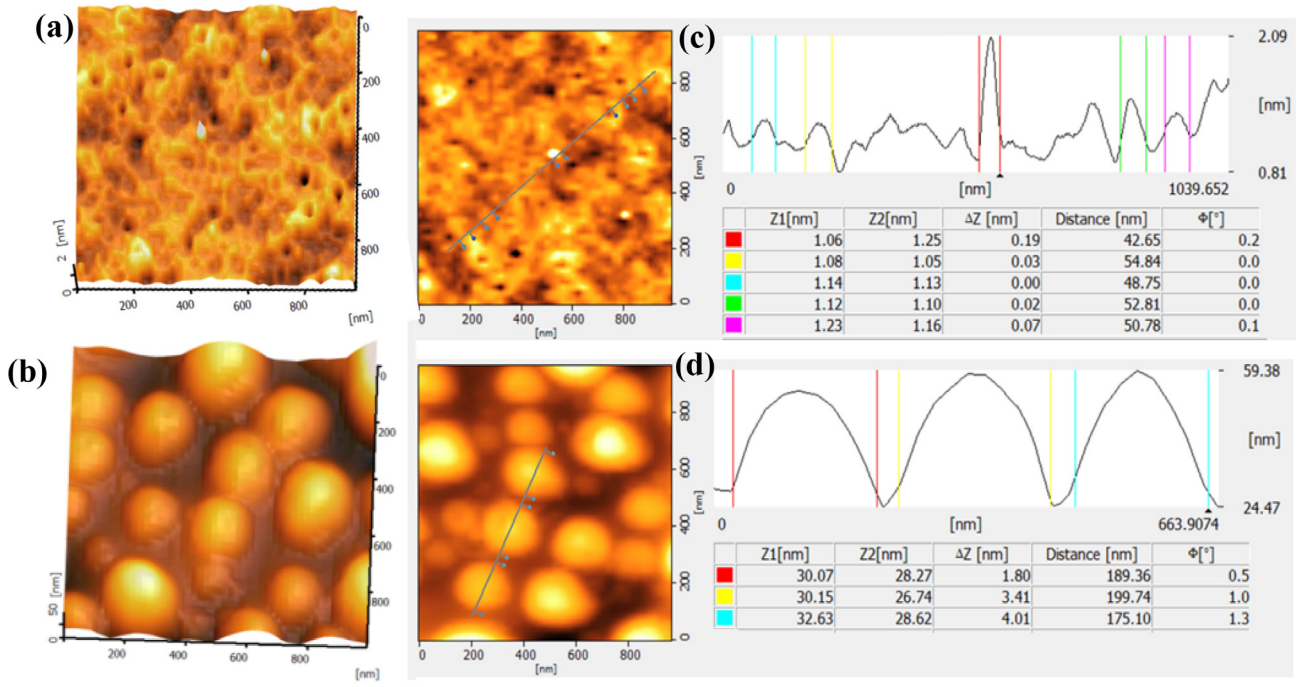

Fig. 3 AFM 3-D micrographs of (a) silica nano-matrix (b) BPB encapsulated silica matrix, (c) 2-D image and line profile of silica nano-matrix (d) 2-D image and line profile of BPB encapsulated silica matrix.

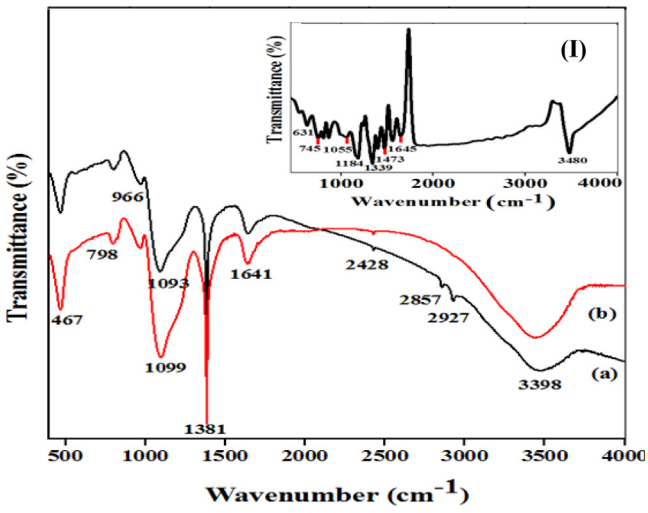

Fig. 4 FTIR spectra of (a) silica nano-matrix (b) BPB encapsulated silica matrix. Inset (I) corresponding to the BPB dye spectrum.

at 2428 cm^{-1}, 2857 cm^{-1}, and 2927 cm^{-1} are associated with typical stretching vibrations of the C—H, which resulted in CH_3— CH_2— from surfactant CTAB [36].

BET multipoint surface analysis shows that silica nano-matrix has a high surface area 477 m^2/g, which reduced to 447 m^2/g after encapsulation, probably BPB species filled the pores within silica nano-matrix and increased the BJH pore diameter. Ritter et al [37] reported that BJH pore diameter increased after encapsulation due to the probability for functional species binding to pore entrance sites increases. BET surface area, pore volume and pore diameter variations of silica nano-matrix before or after encapsulation are summarized in Table 2. Thus, high surface areas, large pore volumes and large pore diameter allow for hosting large objects and anchoring molecular functions, i.e., fast mass diffusion and transfer process that is desirable for separation, catalysis, drug delivery, supercapacitors, adsorption studies and sensing applications [35].

Fig. 5 shows N_2 adsorption and desorption isotherms of silica and BPB encapsulated silica patterns. The normalized pore diameter distributions are shown in the insets of Fig. 5(a, b). The sorption isotherm of silica is similar in shape to type IV according to IUPAC classification terms referring to the mesoporous character of the materials as documented in the literature [38]. The isotherms are characterized by the sharp step of capillary condensation. The resultant nano-patterns show H_2 type hysteresis loops corresponding to materials with interconnected non-uniform pore size system according to IUPAC classification. The hysteresis cycle of BPB encapsulated silica matrix [Fig. 5(b)] is narrower than silica nano-matrix [Fig. 5 (a)], implying the wide pore openings than silica nano-matrix [Fig. 5-inset (II)], i.e., the pore size distribution is not wide in silica matrix [Fig. 5-inset (I)]. Moreover, BPB encapsulated silica matrix sorption isotherm is almost same as silica nano-matrix. This fact implies that the pore systems were preserved in the intact regions and collapsed fully, i.e., the contribution of the transition zones to the porosity [39].

4.2. Thermal analysis

Fig. 6(a, b) shows the thermogravimetric analysis (TGA) plots of the CTAB modified-silica nano-matrix and BPB encapsulated silica matrix in the temperature range of 30 °C–1000 °C. Generally, the weight loss below 100 °C is ascribed to the release of adsorbed water, and the weight loss above 250 °C is attributed to the decomposition of an organic moiety in the sample [40]. In case of silica nano-matrix, mass weight loss occurred in three steps. The first mass weight at ~20.83% within a temperature range of 30 °C–200 °C, corresponds to the adsorbed water molecules.

In the second step, a temperature range of 220 °C–410 °C, the weight loss is reduced and observed around 11.22%, which can be attributed to the surfactant CTAB moieties' decomposition. In the third step, thermal decomposition of escaped organic moieties within the silica matrix walls was observed about 4.67% within a temperature range of 420 °C–1000 °C or more likely to condensation of silanols. The first order mathematical derivative operation DTA was applied to silica sample, to pin-out the weight loss corresponding to the temperature. The prominent peak ~320 in silica matrix is observed due to the surfactant species' decomposition. Furthermore, BPB encapsulated silica matrix shows a high weight loss ~46.18% within the temperature range of 30 °C–130 °C, due to the removal of physically absorbed water molecules. As documented in literature [41], H_2O molecules are highly polar which possibly leads to the multilayer adsorption. Therefore, a high weight loss is observed within the temperature range of 30 °C–130 °C. The adsorption of water molecules on the siloxane groups Si atoms is due to the Van de Waals force, which is significant in very small pores due to the micropore confinement and the large silica surface. However, no further weight loss was observed until 1000 °C, which is attributed to the strong bonding between dye species and silica matrix particles. Thermal stability findings suggest that CTAB-modified silica particles after encapsulation process improve the thermal stability. In DTA thermograph, the endothermic peaks within the range of 30 °C–150 °C correspond to the evaporation of solvents and water molecules. However, after encapsulation, there is no peak observed within the range of 120 °C–1000 °C, suggesting the little dye was incorporated with silica, and instead a phase separated CTAB/dye phase formed.

Table 2 Surface area, pore volume and BJH pore diameter distribution of silica and BPB encapsulated silica matrix.

Samples	Surface area (m^2/g)	Pore Volume (cm^3/g)	BJH Pore diameter (Å)
CTAB modified silica nano-matrix	477	0.93	75.62
BPB encapsulated silica nano-matrix	447	0.95	84.60

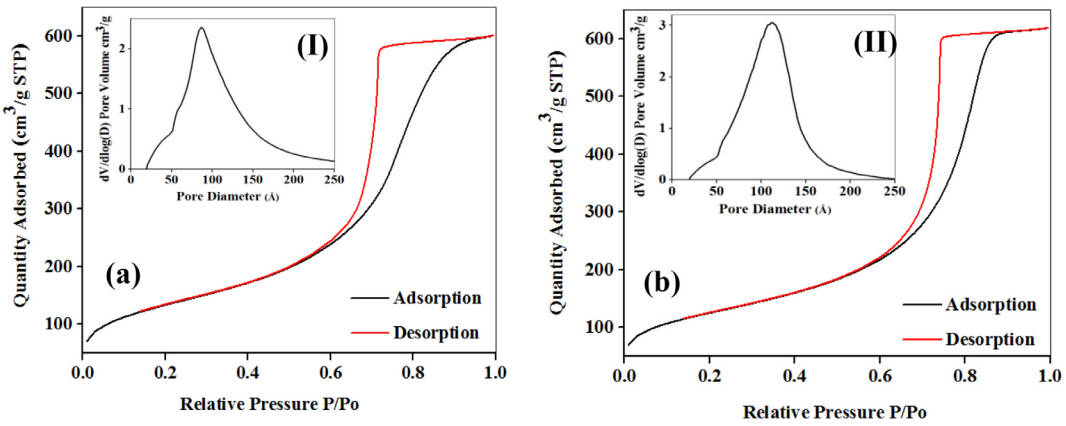

Fig. 5 N_2 adsorption-desorption isotherm (a) silica nano-matrix (b) BPB encapsulated silica matrix inset (I) is pore size distribution of silica nano-matrix and inset (II) is adsorption pore size distribution of BPB encapsulated silica matrix.

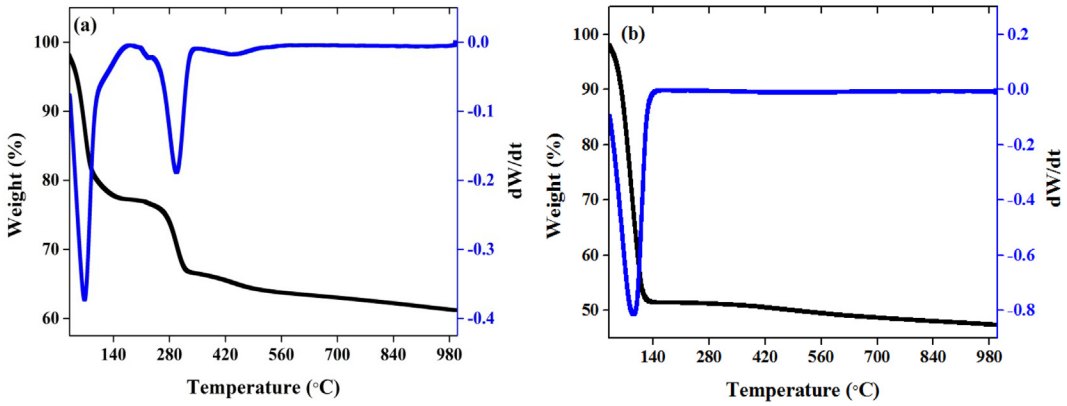

Fig. 6 Weight (%) versus temperature (°C) and [dW/dT] (a) silica nano-matrix (b) BPB encapsulated silica matrix.

4.3. Optical analysis

Fig. 7-I(a, b) shows the transmittance spectra of silica nano-matrix and BPB encapsulated silica matrix at room temperature within the range of 320 nm–700 nm. In Fig. 7-I(a), 82% transmission is observed in silica nano-matrix at 550 nm. However, after encapsulation, two prominent absorption bands were observed at ~435 nm and ~608 nm [Fig. 7-I (b)], may be due to the cluster formation. The observed transmission is ~83% at 550 nm in BPB encapsulated sample. As documented

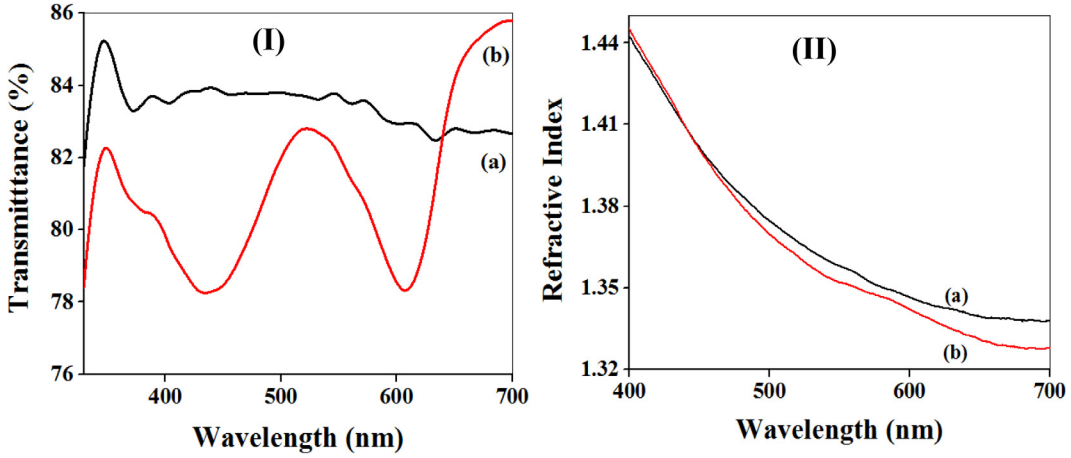

Fig. 7 (I) Transmission spectra of (a) silica nano-matrix (b) BPB encapsulated silica nano-matrix. (II) Dispersion of refractive index (a) silica nano-matrix (b) BPB encapsulated silica nano-matrix.

in literature several parameters such as material's composition, the degree of polymerization, water absorption, sol stability, particle size and the refractive index of the components affect the transmission [42]. Moreover, the transmittance of composite changes according to its ability to transmit light to its components and particle sizes [43].

Refractive index was calculated by the Fresnel formula (reflection data was taken by UV–Vis spectroscopy) within the range of 400 nm–700 nm. The refractive index profiles for silica nano-matrix and BPB encapsulated silica matrix are illustrated in Fig. 7-II(a, b). Low value of refractive index 1.36 at 550 nm was observed for silica nano-matrix and 1.35 at 550 nm for BPB encapsulated silica matrix. A high degree of porosity is responsible for low refractive index or probably voids between the particles are responsible for the reduction in refractive index of the coating, as observed in our previous studies [44].

4.4. Sensing analysis

The output intensity configuration employed relies on evanescent wave (EW) interactions between the optical fiber guided radiation and BPB encapsulated silica nano-matrix deposited sensing cladding [Fig. 8(a)]. Furthermore, the calculated refractive index of the sensitive layer is 1.36 which determines the evanescent field; lower than the refractive index of the fiber 1.45. In EW based fiber optic sensor, the optical signals are guided through fiber by total internal reflection. As a result, the amount of light guided is modulated by refractive indices of the various media i.e. cladding and core. Basically in an evanescent field, when the light is guided in an optical fiber, a fraction of the radiation extends a short distance from the guiding region into the medium of the lower refractive index that surrounds it [45]. Fig. 8(a) shows that when pH increases the intensity also increases until pH 9, whereas when pH further increases up to pH 12, it decreased. The possible reason is when absorption of the analyte (coating) by the evanescent field around the sensing fiber becomes higher the output intensity gradually decreases. The evanescent field reacts mightily with the coating because when the wavelength increases the penetration depth becomes large. Therefore, when evanescent field interacts with the BPB dye encapsulated silica film on the fiber optic core, absorption change of the deposited films occurred due to a change in pH of the external environment and dye response is registered as a change in the spectral transmission (output intensity) of the fiber [Fig. 8(a)]. The fingerprints of coated layer and highest peak position corresponding to pH 9 at 454 nm as shown in Fig. 8(a)-inset. Since, the BPB dye is not fluorescent the encapsulation phenomenon could be checked by transmission measurements. Moreover, Cao et al. [46] reported that the optical absorbance of the solution caused the change in optical transmission properties resulting in the light absorption phenomenon on fiber optical structure when the radiation losses increase.

Fig. 8(b) shows the response of the device for different pH solutions within 1–12 at 454 nm. Linear relationship is observed by varying the pH values 1–9, however, at high pH values 10–12 the intensity response is decreased. The value of sensitivity is calculated as 18.37 counts/pH with repeatability of 78% [Fig. 8(b)], suggesting that the sensor has a good level of compatibility between silica pores and BPB dye species up to pH 9.

Fig. 9(a) shows the average/mean time response of sensing device within pH ranges 1–12 after three measurements. It can be clearly seen from Fig. 9(a) that prepared sensing device is more responsive toward basic pHs $\sim$ 0.25 s than acidic pHs $\sim$ 0.85 s. This fast responsive coated fiber sensor is a significant improvement over previous reported work [Table 1], where stated response times were in the order of several minutes to 5 s [22–29].

Additionally, in the buffer solution, the BPB indicator dye is well known for changing color from yellow (acid) to blue (alkaline). The color variations in coated fiber in different pH solutions are shown in Fig. 9(b). The change in color also leads to an attenuation of the guided light at a particular wavelength of 454 nm. The attenuation of the guided light is caused by absorption of its evanescent part in the sensitive layer. The findings resulted in that the indicator species was still reactive after encapsulation, and changed the pH toward H^+ and OH^- reactions.

For repeatability/reproducibility analysis, the prepared sensor fiber was treated three times with two pH solutions 9 and

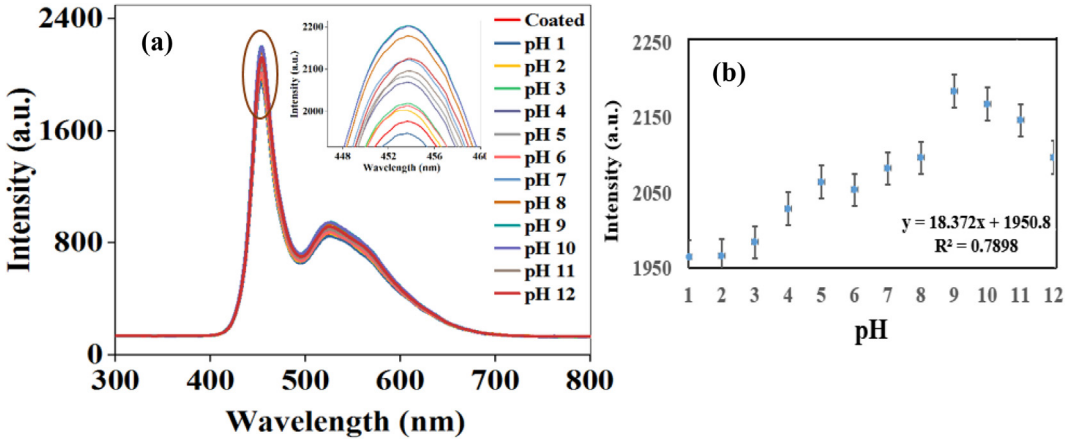

Fig. 8 (a) illustrates the spectra of BPB encapsulated silica nano-matrix coated fiber within different pH solutions 1–12 under a white LED light source. Inset is the zoomed view of marked region in (a), whereas, (b) is the response curve of the coated fiber for pH values 1–12 at 454 nm.

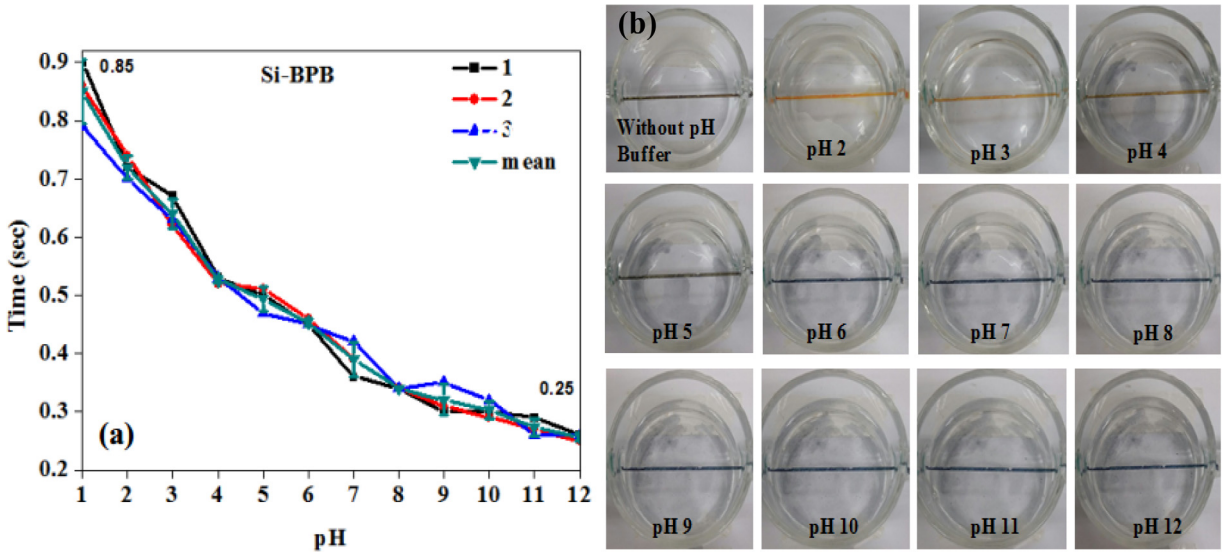

Fig. 9 (a) Response time graph vs. pH 1–12, whereas, (b) color variations of coated fiber without buffer solution and within different pH solutions 2–12 (Digital pic).

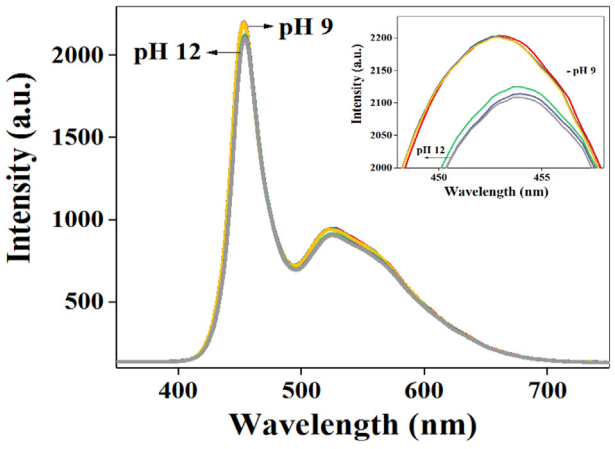

Fig. 10 optical spectra of BPB encapsulated silica matrix coated fiber corresponding to repeatability/reproducibility at two pHs solutions 9 and 12. Inset is zoomed area of highest peaks.

12 [Fig. 10], and it was observed that the response was almost the same in different periods of time (after every 30 min) to the same pH values 9 and 12. A repeatable response in all cases of measurements, suggesting the accuracy/stability of the device. The inset in the Fig. 10 is the zoomed view of marked area on the spectra.

The reliability of the prepared sensing device was validated in practical applications like the basicity of household ammonia and borax solution. The pH was estimated by prepared sensor and cross-checked with digital pH meter (HANNA), as shown in Fig. 11(a, b). Firstly, the pH of household ammonia ~11.9 and borax solution ~9.2 was measured by digital pH meter and then spectrum of household ammonia and borax solution recorded with the prepared device [Fig. 11 (a, b)]. The spectrum of household ammonia and borax solution was almost the same for pH 12 and pH 9, respectively with a negligible error. It suggests that prepared device is potentially suitable for practical applications.

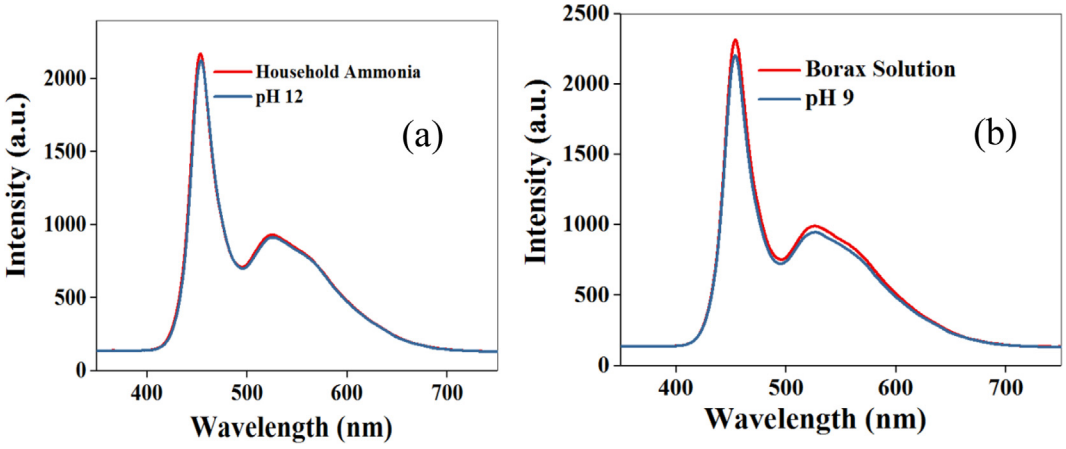

Fig. 11 Optical spectra of (a) household ammonia and (b) borax solution.

5. Conclusion

BPB dye was successfully encapsulated into CTAB modified silica nano-matrix via sol–gel method at low temperature. Sol–gel based silica matrix was obtained with the combination of hydrolysis and condensation reactions of the metal alkoxides which strictly interconnected with indicator species and in this way host–guest network was obtained at room temperature. BPB encapsulated silica matrix was investigated for surface morphology and it was observed that CTAB modified silica particles' dispersal state and thermal stability improved after encapsulation probably due to good interaction of BPB dye species with silica nano-matrix particles. Silica particles were well-dispersed and arranged orderly after encapsulation process. In particular, the surface roughness value decreased when the BPB dye was encapsulated into the silica nano-matrix. Considering the well-ordered stable surface, low roughness, high surface area, higher thermal stability, and low refractive index value it can be widely used for sensing. Because higher surface area and lower refractive index in sensitive regions allows lower limits of detection in pH sensing. Sensing analysis suggested that prepared device was fast responsive 0.25 s in basic pH, reversible, and stable for repeated measurements in different pH solutions 1–12 without any significant leaching traces. So, it is concluded that the combination of fiber optic with the encapsulation of BPB in CTAB modified silica matrix can be successfully used to enhance the dynamic pH range and has potential for practical applications.

Acknowledgements

Authors acknowledge the financial support provided by the Universiti Teknologi Malaysia, through RMC under the Postdoctora Manuscript has been modified. Fellowship for the performance and management of the project. Corresponding author is grateful to the Malaysian Ministry of Education through the FRGS fund with vote 03E89.

References

[1] J. Tang, J. Liu, C. Li, Y. Li, M.O. Tade, S. Dai, Y. Yamauchi, Synthesis of nitrogen-doped mesoporous carbon spheres with extra large pores through assembly of di block copolymer micelles, Angew. Chem. Int. Ed. 54 (2015) 588–593.

[2] H. Ataee-Esfahani, Y. Nemoto, L. Wang, Y. Yamauchi, Rational synthesis of Pt spheres with hollow interior and nanosponge shell using silica particles as template, Chem. Commun. 47 (2011) 3885–3887.

[3] V. Malgra, H. Ataee-Esfahani, H. Wang, B. Jiang, C. Li, K. Wu, J.H. Kim, Y. Yamauchi, Nanoarchitectures for mesoporous metals, Adv. Mater. (2015).

[4] D. Blanc, W. Zhang, C. Massard, J. Mugnier, Synthesis and characterisation of tantalum-incorporating silica hybrid sol–gel thin films for optical applications, Opt. Mater. 28 (2006) 331–335.

[5] J. Wang, Z.H. Shah, S. Zhang, R. Lu, Silica-based nanocomposites via reverse microemulsions: classifications, preparations, and applications, Nanoscale 6 (2014) 4418.

[6] W. Scharti, Current directions in core–shell nanoparticle design, Nanoscale 2 (2010) 829–843.

[7] M.V. Kahraman, M. Kugua, Y. Menceloglu, N. Kayaman-Apohan, A. Gungor, The novel use of organo alkoxy silane for the synthesis of organic–inorganic hybrid coatings, J. Non-Cryst. Solids 352 (21–22) (2006) 2143–2151.

[8] S. Karatas, C. Kızılkaya, N. Kayaman-Apohan, A. Gungor, Preparation and characterization of sol–gel derived UV-curable organo-silica–titania hybrid coatings, Prog. Org. Coatings 60 (2007) 140–147.

[9] S. Islam, N. Bidin, S. Riaz, S. Naseem, Sol–gel based phenolphthalein encapsulated heterogeneous silica–titania optochemical pH nanosensor, J. Ind. Eng. Chem. 34 (2016) 258–268.

[10] K.K. Coti, M.E. Belowich, M. Liong, M.W. Ambrogio, Y.A. Lau, H.A. Khatib, J.I. Zink, N.M. Khashab, J.F. Stoddart, Mechanised nanoparticles for drug delivery, Nanoscale 1 (2009) 16–39.

[11] D. Avnir, D. Levy, R. Reisfeld, The nature of the silica cage as reflected by spectral changes and enhanced photostability of trapped rhodamine, J. Phys. Chem. 88 (1984) 5956–5959.

[12] A. Urrutia, J. Goicoechea, F.J. Arregui, Optical fiber sensors based on nanoparticle-embedded coatings, J. Sensors 2015 (2015), 18 pages 805053.

[13] R. Aneesh, S.K. Khijwania, Zinc oxide nanoparticle based optical fiber humidity sensor having linear response throughout a large dynamic range, Appl. Optics 50 (27) (2011) 5310–5314.

[14] P.J. Rivero, A. Urrutia, J. Goicoechea, F.J. Arregui, I.R. Matías, Humidity sensor based on silver nanoparticles embedded in a polymeric coating, Int. J. Smart Sensing Intell. Syst. 5 (1) (2012) 71–83.

[15] R.N. Mariammal, K. Ramachandran, B. Renganathan, D. Sastikumar, On the enhancement of ethanol sensing by CuO modified SnO_2 nanoparticles using fiber-optic sensor, Sens. Actuators, B 169 (2012) 199–207.

[16] B. Renganathan, D. Sastikumar, S.G. Raj, A.R. Ganesan, Fiber optic gas sensors with vanadium oxide and tungsten oxide nanoparticle coated claddings, Opt. Commun. 315 (2014) 74–78.

[17] L.R. Shobin, D. Sastikumar, S. Manivannan, Glycerol mediated synthesis of silver nanowires for room temperature ammonia vapor sensing, Sens. Actuators, A 214 (2014) 74–80.

[18] B. Renganathan, D. Sastikumar, G. Gobi, N.R. Yogamalar, A. C. Bose, Gas sensing properties of a clad modified fiber optic sensor with Ce, Li and Al doped nanocrystalline zinc oxides, Sens. Actuators, B 156 (1) (2011) 263–270.

[19] S. Kodaira, S. Korposh, S.-W. Lee, W. J. Batty, S. W. James, and R. P. Tatam, Fabrication of highly efficient fibre-optic gas sensors using SiO2/polymer nanoporous thin films, in Proceedings of the 3rd International Conference on Sensing Technology (ICST '08), 2008, 481–485.

[20] P.S. Kumar, C.P.G. Vallabhan, V.P.N. Nampoori, V.N.S. Pillai, P. Radhakrishnan, A fibre optic evanescent wave sensor used for the detection of trace nitrites in water, J. Opt. A: Pure Appl. Opt. 4 (2002) 247–250.

[21] Thesis by David Gerard O'Keeffe, Development of Fibre Optic Evanescent-Wave Fluorescence-Based Sensors, Dublin City University, 1995.

[22] M. Zolkapli, S. Saharudin, S.H. Herman, W.F.H. Abdullah, A numerical analysis of various pH level for fiber optic pH sensor based on bromophenol blue in silica, Int. J. Electr. Electron. Syst. Res. 9 (2016).

[23] B.D. Gupta, D.K. Sharma, Evanescent wave absorption based fiber optic pH sensor prepared by dye doped sol-gel immobilization technique, Opt. Commun. 140 (1–3) (1997) 32–35.

[24] John E. Lee, S. Scott Saavedra, Evanescent sensing in doped sol-gel glass films, Anal. Chim. Acta 285 (1994) 265–269.

[25] F.B.M. Suah, M. Ahmad, M.N. Taib, applications of artificial neural network on signal processing of optical fibre pH sensor based on bromophenol blue doped with sol–gel film, Sens. Actuators B: Chem. 90 (1–3) (2003) 182–188.

[26] C. Dafu, Optical-fibre pH sensor, Sens. Actuators B: Chem. 12 (1) (1993) 29–32.
[27] B.D. MacCraith, C.M. McDonagh, G. OKeeffe, A.K. McEvoy, T. Butler, F.R. Sheridan, Sol–gel coatings for optical chemical sensors and biosensors, Sens. Actuators, B 29 (1–3) (1995) 51–57.
[28] R.-L. Alvarado-Mendez, R. Andrade-Lucio, D. Hernandez-Cruz, R.A. Lessard, J.G. Avina-Cervantes, Design and characterization of pH sensor based on sol–gel silica layer on plastic optical fiber, Sens. Actuators B: Chem. 106 (2) (2005) 518–522.
[29] B.D. Gupta, D.K. Sharma, Evanescent wave absorption based fiber optic pH sensor prepared by dye doped sol–gel immobilization technique, Opt. Commun. 140 (1–3) (1997) 32–35.
[30] W.A.A. Twej, F.J. Al-maliki, B.T. Chiad, Study of R-molar ratio effect on the transformation of tetraethylorthosilicat precursor to gels in sol-gel technique, Baghdad Sci. J. 6 (3) (2009) 590–595.
[31] Y. Fatieiev, J.G. Croissant, K. Julfakyan, L. Deng, D.H. Anjum, A. Gurinov, N.M. Khashab, Enzymatically degradable hybrid organic–inorganic bridged silsesquioxane nanoparticles for in vitro imaging, Nanoscale 7 (2015) 15046.
[32] S. Liang, K. Shephard, D.T. Piercea, Julia Xiaojun Zhao, Effects of a nanoscale silica matrix on the fluorescence quantum yield of encapsulated dye molecules, Nanoscale 5 (2013) 9365.
[33] A. Auger, J. Samuel, O. Poncelet, O. Raccurt, A comparative study of non-covalent encapsulation methods for organic dyes into silica nanoparticles, Nanoscale Res. Lett. 6 (2011) 328.
[34] M. Veerapandian, K. Yun, Methylene blue dye coated silver–silica nanoparticles with dual functionality fabricated by injection pump and ultrasonochemistry, Mater. Res. Bull. 48 (2013) 1817–1823.
[35] R. Rakshit, E. Khatun, M. Pal, S. Talukdar, D. Mandal, P. Saha, K. Mandal, Influence of functional groups of dye on the adsorption behavior of CoFe2O4 nano-hollow spheres, New J. Chem. 41 (2017) 9095–9102.
[36] X. Ma, S. Kim, Synthesis and Characterisation of Silica/Polyamide-Imide Composite Film for Enamel Wire, INTECH, 2012, chapter 28, DOI: 10.5772/35719.
[37] H. Ritter, J.H. Ramm, D. Brühwiler, Influence of the structural properties of mesoporous silica on the adsorption of guest molecules, Materials 3 (2010) 4500–4509.
[38] X. Pang, F. Tang, Morphological control of mesoporous materials using inexpensive silica sources, Microporous Mesoporous Mater. 85 (2005) 1–6.
[39] E. Albert, P. Basa, A. Deak, A. Nemeth, Z. Osvath, G. Safran, Z. Zolnai, Z. Horvolgyi, N. Nagy, Introducing nanoscaled surface morphology and percolation barrier network into mesoporous silica coatings, RSC Adv. 5 (2015) 60041.
[40] X. Zhang, Y. Zhao, S. Xie, L. Sun, Fabrication of functionalized porous silica nanoparticles and their controlled release behavior, J. Drug Delivery Sci. Technol. 37 (2017) 38–45.
[41] V.V. Turov, I.F. Mironyuk, Adsorption layers of water on the surface of hydrophilic, hydrophobic and mixed silicas, Colloids Surf. A 134 (1998) 257–263.
[42] X. Wang, G. Wu, B. Zhou, Optical constants of crystallized TiO2 coatings prepared by sol-gel process, Materials 6 (2013) 2819–2830.
[43] R.S. Queiroz, J.P.M.d. Lima, D.A.M.P. Malta, A.N.d.S. Rastelli, A. Cuin, S.d.T.P. Neto, Changes on transmittance mode of different composite resins, Mater. Res. 12 (2) (2009) 127–132.
[44] S. Islam, N. Bidin, Z. Haider, S. Riaz, S. Naseem, M.A. Saeed, F.M. Marsin, Sol–gel-based single and multilayer nanoparticle thin films on low-temperature substrate poly-methyl methacrylate for optical applications, J. Sol-Gel Sci. Technol. 77 (2016) 396–403.
[45] T.M. Butler, B.D. MacCraith, C. McDonagh, Leaching in sol–gel-derived silica films for optical pH sensing, J. Non-Cryst. Solids 224 (1998) 249–258.
[46] W. Cao, Y. Duan, Optical fiber-based evanescent ammonia sensor, Sens. Actuators, B 110 (2) (2005) 252–259.